JPE Journal of Photonics for Energy

RESEARCH PAPER

Effects of defect density, minority carrier lifetime, doping density, and absorber-layer thickness in CIGS and CZTSSe thin-film solar cells

Faiz Ahmad,[a,*] **Benjamin J. Civiletti,**[b] **Peter B. Monk,**[c] **and Akhlesh Lakhtakia**[a]
[a]The Pennsylvania State University, Department of Engineering Science and Mechanics,
NanoMM–Nanoengineered Metamaterials Group, University Park, Pennsylvania, United States
[b]Augustana College, Department of Mathematics and Computer Science, Rock Island, Illinois, United States
[c]University of Delaware, Department of Mathematical Sciences, Newark, Delaware, United States

ABSTRACT. Detailed optoelectronic simulations of thin-film photovoltaic solar cells (PVSCs) with a homogeneous photon-absorber layer made of with CIGS or CZTSSe were carried out to determine the effects of defect density, minority carrier lifetime, doping density, composition (i.e., bandgap energy), and absorber-layer thickness on solar-cell performance. The transfer-matrix method was used to calculate the electron-hole-pair (EHP) generation rate, and a one-dimensional drift-diffusion model was used to determine the EHP recombination rate, open-circuit voltage, short-circuit current density, power-conversion efficiency, and fill factor. Through a comparison of limited experimental data and simulation results, we formulated expressions for the defect density in terms of the composition parameter of either CIGS or CZTSSe. All performance parameters of the thin-films PVSCs were thereby shown to be obtainable from the bulk material-response parameters of the semiconductor, with the influence of surface defects being small enough to be ignored. Furthermore, unrealistic values of the defect density (equivalently, minority carrier lifetime) will deliver unreliable predictions of the solar-cell performance. The derived expressions should guide fellow researchers in simulating the graded-bandgap and quantum-well-based PVSCs.

[DOI: 10.1117/1.JPE.13.025502]

Keywords: thin-film solar cell; Shockley–Read–Hall recombination; defects/traps density; carrier lifetimes

Paper 23006G received Jan. 12, 2023; revised Apr. 28, 2023; accepted May 10, 2023; published Jun. 2, 2023.

1 Introduction

Thin-film photovoltaic solar cells (PVSCs) are promising alternatives to crystalline-silicon solar cells, in part due to significantly reduced material consumption and in part because of reduced manufacturing costs.[1–3] PVSCs could be deployed on both exterior and interior surfaces of buildings to harvest direct as well as diffuse solar energy and to recycle electrically generated light in habitable spaces. Compound semiconductors, such as $\mathrm{CuIn}_{1-\xi}\mathrm{Ga}_{\xi}\mathrm{Se}_2$ (CIGS) and $\mathrm{Cu}_2\mathrm{ZnSn}(\mathrm{S}_{\xi}\mathrm{Se}_{1-\xi})_4$ (CZTSSe) are very attractive, because the bandgap energy E_g, and therefore the harvested portion of the optical spectrum, can be compositionally engineered as indicated by the composition parameter $\xi \in [0,1]$.[4]

The major obstacle to the large-scale production of CIGS thin-film PVSCs is the scarcity of indium.[5] CZTSSe contains earth-abundant materials,[4] but CZTSSe thin-film PVSCs have a low

---

*Address all correspondence to Faiz Ahmad, fua26@psu.edu

1947-7988/2023/$28.00 © 2023 SPIE

power-conversion efficiency η due to (i) the low open-circuit voltage V_{oc} caused by more bandtail states[6,7] and (ii) the high bulk and interfacial electron-hole recombination rates.[8–11] Current research efforts to improve the efficiencies of thin-film PVSCs include but are not limited to the following: light-trapping strategies to harvest more photons,[12–15] new semiconductors with the more efficient conversion of photons into charge carriers,[16] bandgap grading of semiconductor layers,[17–22] and back-surface passivation.[23] Because experiments on different PVSC geometries can be costly and time-consuming, modeling and simulation can help in understanding the device physics underlying η.[6,17–20,24–31] Diverse simulation packages are available to model and study performance parameters of thin-film PVSCs.[32] Most simulation packages use the drift-diffusion equations to simulate charge-carrier transport,[33,34] in which the input is the electron-hole pair (EHP) generation rate G. This quantity is obtained from optical calculations that employ either the simple Bouguer–Beer–Lambert law[35–38] or the rigorous transfer-matrix method.[39–41] Along with the computational schemes for optics and charge-carrier transport, material-response parameters must be carefully chosen to simulate representative experimental solar cells and to understand, evaluate, and improve the solar-cell performance. A poor choice of material-response parameters without cross-comparison with experimental results can lead to inadequate guidelines for experimentalist colleagues.

Surface electron-hole recombination has a minimal effect on the performance of CIGS and CZTSSe thin-film PVSCs, the performance parameters of which can be adequately simulated using only the bulk material-response parameters.[6,24,30] Charge-carrier transport in bulk materials involves three nonlinear recombination processes: Shockley–Read–Hall (SRH), radiative, and Auger.[30,33,34] The most complicated of these three processes (especially in the choice of defect density or trap density N_{f}, electron lifetime τ_{n}, and hole lifetime τ_{p}) is the SRH recombination process. This process can be implemented using either the defect density or the carrier lifetimes (especially, the minority carrier lifetime). But in either case, the process is dictated by the defect density chosen for the simulation,[42] and an inadequate choice can lead to a poor prediction of the device performance. With increased interest in bandgap-graded and quantum-well CIGS and CZTSSe thin-film PVSCs,[6,17,18,43–52] a knowledge of defect density and carrier lifetimes in relation to E_{g} (and therefore ξ) is a must.

In a CIGS solar cell, defects in the p-type CIGS photon-absorber layer constitute deep traps for electrons (minority carriers). Higher gallium content (i.e., higher ξ) leads to higher N_{f} and lower τ_{n}, and some nonlinear fits of N_{f} to ξ have been proposed.[25,31] However, a systematic study of the performance parameters of a solar cell with a homogeneous CIGS layer versus ξ can establish N_{f} and τ_{n} for simulating graded-bandgap[46–49] and quantum-well[50–52] CIGS solar cells.

Similarly, the p-type compound semiconductor CZTSSe also has E_{g}-dependent N_{f}, and higher sulfur content leads to higher N_{f} and lower τ_{n}. The effects of defect density and carrier lifetimes on the performance of CZTSe (i.e., $\xi = 0$) and CZTS (i.e., $\xi = 1$) thin-film PVSCs have been theoretically established,[53,54] but not for $\xi \in (0,1)$.

We report here the effects of defect density and minority carrier lifetime on the performance of CIGS and CZTSSe thin-film PVSCs with a homogeneous photon-absorber layer to provide guidance to select N_{f} (or, equivalently, τ_{n}) as a function of ξ for optoelectronic simulation using the standard equations of optics and electronics.[30,33,34] In addition, we varied the doping density N_{d} in the CIGS or CZTSSe photon-absorber layer as a function of E_{g} to see any significant effects on the performances of both types of cells. (The doping density $\mathrm{N_d} = \mathrm{N_D}\text{-}\mathrm{N_A}$ is the excess of the donor density $\mathrm{N_D}$ over the acceptor density $\mathrm{N_A}$. Whereas $\mathrm{N_D} = 0$ in a p-type semiconductor, $\mathrm{N_A} = 0$ in an n-type semiconductor.) Because the minority carrier lifetime τ_{n} varies with ξ, there will be a different minority-carrier diffusion length for different values of E_{g}, and concurrently, the thickness L_{s} of the photon-absorber layer for maximum η will vary with E_{g}. Therefore, we also report the effects of ξ and L_{s} on the performances of both types of thin-film PVSCs. The performance parameters include η, V_{oc}, the short-circuit current density J_{sc}, and the fill factor FF.

This paper is organized as follows. Section 2 on the optoelectronic simulation of thin-film PVSCs is divided into three subsections. A description of both solar cells is presented in Sec. 2.1; the optical calculations are discussed in Sec. 2.2; and the electrical description of the solar cell and the electrical computations are described in Sec. 2.3. Numerical results on CIGS thin-film PVSCs are presented and discussed in Sec. 3.1, and those on CZTSSe thin-film PVSCs are in Sec. 3.2. The paper ends with concluding remarks in Sec. 4.

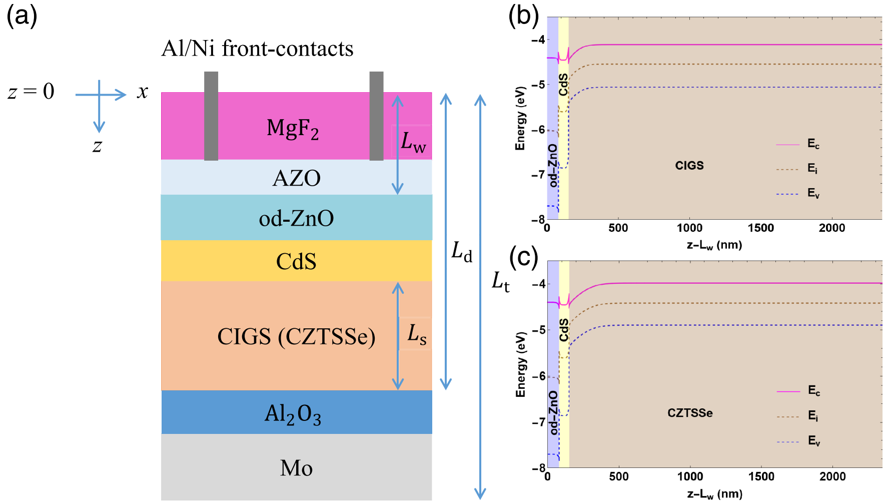

Fig. 1 (a) Schematic of a CIGS (or CZTSSe) thin-film PVSC. (b) Schematic band diagram in the od-ZnO/CdS/CIGS region when $\xi = 0$. (c) Schematic band diagram in the od-ZnO/CdS/CZTSSe region when $\xi = 0$. The conduction and valence band edge energies are represented by E_c and E_v, respectively, and E_i is the intrinsic energy.

2 Optoelectronic Simulation

2.1 Solar Cell Description

Figure 1(a) shows a schematic of a $\mathrm{MgF_2/AZO/od\text{-}ZnO/CdS/CIGS(CZTSSe)/Al_2O_3/Mo}$ thin-film PVSC. The aluminum/nickel grid used as a front contact in the PVSC is typically deposited using an evaporation technique.[55] The 110-nm-thick MgF_2 layer acts as an antireflection coating. Electrons are collected in the 100-nm-thick aluminum-doped zinc oxide (AZO) layer as AZO is a transparent conducting oxide (TCO). Other commonly used TCOs are tin oxide, indium tin oxide, zinc oxide, and cadmium oxide.[56,57] The 80-nm-thick layer of oxygen-deficient zinc oxide (od-ZnO) and the 70-nm-thick layer of cadmium sulfide (CdS) function as n-type semiconductors. The photon-absorber layer of p-type CIGS (or CZTSSe) is of thickness $L_s \le 2200$ nm, the 20-nm-thick Al_2O_3 layer is needed for passivation, and the 500-nm-thick Mo layer serves as both the back-contact and an optical reflector. The illuminated surface of the solar cell is the plane $z = 0$, and the total thickness of the solar cell is denoted by L_t.

Schematic band diagrams of the od-ZnO/CdS/CIGS and od-ZnO/CdS/CZTSSe regions of the thin-film PVSC are shown in Figs. 1(b) and 1(c), respectively. The conduction and valence band edge energies are represented by E_c and E_v, respectively, and $\mathsf{E}_i = (\mathsf{E}_c + \mathsf{E}_v)/2$ is the intrinsic energy in the middle of the bandgap.

2.2 Optical Calculations

The transfer-matrix method[39–41] was used to calculate the electric field phasor $\mathbf{E}(z,\lambda_0) = E_x(z,\lambda_0)\hat{\mathbf{u}}_x$ everywhere inside the solar cell as a result of illumination by a monochromatic plane wave normally incident on the plane $z = 0$ from the half-space $z < 0$, where $\hat{\mathbf{u}}_x$ is the unit vector parallel to the x axis and λ_0 is the free-space wavelength. The electric field phasor of the incident plane wave was taken as

$$\mathbf{E}_{\mathrm{inc}}(z,\lambda_0) = E_0\hat{\mathbf{u}}_x \exp\left(i2\pi\frac{z}{\lambda_0}\right), \tag{1}$$

where $E_0 = 4\sqrt{15\pi}\ \mathrm{V\,m^{-1}}$. Standard electromagnetic boundary conditions were enforced on the planes $z = 0$ and $z = L_t$ to match the internal field phasors to the incident, reflected, and transmitted field phasors, as appropriate. Note that the transfer-matrix method provides an exact solution of the Maxwell equations, whereas the simple Bouguer–Beer–Lambert law[35–38] is an approximation.

With the assumption that every absorbed photon excites an EHP, the EHP generation rate was calculated as

$$G(z) = \frac{\eta_0}{\hbar E_0^2} \int_{\lambda_{0,\min}}^{\lambda_{0,\max}} \mathrm{Im}\{\varepsilon(z,\lambda_0)\} |E_x(z,\lambda_0)|^2 S(\lambda_0) \mathrm{d}\lambda_0 \tag{2}$$

in the region $L_w < z < L_d$ containing the od-ZnO, CdS, and CIGS or CZTSSe layers. Here, η_0 is the intrinsic impedance of free space, $\hbar$ is the reduced Planck constant, $S(\lambda_0)$ is the AM1.5G solar spectrum,[58] $\varepsilon(z,\lambda_0)$ is the permittivity, $\lambda_{0,\min} = 300$ nm, and $\lambda_{0,\max} = (1240/\mathsf{E}_g)$ eV nm. Spectrums of the real and imaginary parts of the relative permittivity $\varepsilon(\lambda_0)/\varepsilon_0$ of MgF_2,[59] AZO,[60] od-ZnO,[61] CdS,[62] CIGS,[63,64] CZTSSe,[65,66] Al_2O_3, and Mo[67] used in our calculations are available in Ref. 30. All layers are homogeneous for the results reported here, and $G(z)$ is a piecewise continuous function of z.

2.3 Electrical Calculations

The region $L_w < z < L_d$ was considered for electrical calculations. As our focus is on modeling the electrical characteristics of the solar cell, not on how it interfaces with an external circuit, both terminals were assumed to be ideal ohmic contacts. We used a one-dimensional drift-diffusion model[33,34,68,69] to investigate the transport of electrons and holes for $z \in [L_w, L_d]$. The solution of the drift-diffusion system yields the electron current density $J_n(z)$, the hole current density $J_p(z)$, and the device current density

$$J_{\mathrm{dev}} = J_n(z) + J_p(z), \quad z \in [L_w, L_d], \tag{3}$$

which is independent of z but is a function of the voltage V_{ext} applied across the planes $z = L_w$ and $z = L_d$. The product $P = J_{\mathrm{dev}} V_{\mathrm{ext}}$ can then be maximized by varying V_{ext} to obtain the maximum power that the solar cell can produce and, hence, the efficiency η for any particular design.

Two major recombination processes involved in the chosen PVSCs are radiative recombination and SRH recombination.[33,34] The radiative recombination rate is given as

$$R_{\mathrm{rad}}(n,p;z) = R_B(z)[n(z)p(z) - n_i^2(z)], \quad z \in [L_w, L_d], \tag{4}$$

where $R_B(z)$ is the radiative recombination coefficient, $n(z)$ is the electron density, and $p(z)$ is the hole density,

$$n_i(z) = \sqrt{N_c(z)N_v(z)} \exp[-\mathsf{E}_g(z)/2k_B T] \tag{5}$$

is the intrinsic charge-carrier density, $N_c(z)$ is the effective density of states in the conduction band, $N_v(z)$ is the effective density of states in the valence band, $k_B = 1.3806 \times 10^{-23}$ J K^{-1} is the Boltzmann constant, and T is the absolute temperature. The SRH recombination rate is given as

$$R_{\mathrm{SRH}}(n,p;z) = \frac{n(z)p(z) - n_i^2(z)}{\tau_p(z)[n(z) + n_1(z)] + \tau_n(z)[p(z) + p_1(z)]}, \quad z \in [L_w, L_d], \tag{6}$$

where $n_1(z)$ and $p_1(z)$ are the electron and hole densities at the trap energy level $\mathsf{E}_T(z)$, respectively. The carrier lifetimes[42]

$$\left.\begin{aligned} \tau_n(z) &= \frac{1}{[\sigma_n(z) v_{th}(z) N_f(z)]} \\ \tau_p(z) &= \frac{1}{[\sigma_p(z) v_{th}(z) N_f(z)]} \end{aligned}\right\} \tag{7}$$

depend on the capture cross sections $\sigma_n(z)$ and $\sigma_p(z)$ for electrons and holes, respectively, and $v_{th}(z)$ is the mean thermal speed for all charge carriers. Because the od-ZnO, CdS, CIGS, and CZTSSe layers are homogeneous, $R_B(z)$, $\mathsf{E}_T(z)$, $n_i(z)$, $n_1(z)$, $p_1(z)$, $\sigma_n(z)$, $\sigma_p(z)$, $v_{th}(z)$, and $N_f(z)$ are piecewise constant functions of z, as is $N_d(z)$ and the electron affinity $\chi(z)$. In contrast, $R_{\mathrm{rad}}(n,p;z)$, $R_{\mathrm{SRH}}(n,p;z)$, $n(z)$, and $p(z)$ are piecewise continuous functions of z.

The carrier lifetimes τ_n and τ_p are often incorporated into the simulations as functions of N_f through Eq. (7); however, τ_n and τ_p can be incorporated directly into the simulations. Arbitrary selection of either the defect density or the carrier lifetimes can lead to either poor representations of experimental solar cells or overestimation of η, as exemplified by Refs. 46, 47, 51, and 52.

All layers in the region $L_w < z < L_d$ are homogeneous, so

- the donor density $N_D(z) = N_D^{od-ZnO}$, the acceptor density $N_A(z) = 0$, and $N_f(z) = N_f^{od-ZnO}$ throughout the od-ZnO layer;
- $N_D(z) = N_D^{CdS}$, $N_A(z) = 0$, and $N_f(z) = N_f^{CdS}$ throughout the CdS layer; and
- $N_D(z) = 0$, $N_A(z) = N_A^s$, and $N_f(z) = N_f^s$ throughout the CIGS or CZTSSe layer.

Numerical values of the material-response parameters (e.g., N_D^{od-ZnO} and R_B^{CdS}) required for the electrical calculations are available in Ref. 30. However, L_s, ξ, N_f^s, and N_A^s were kept as variables for optoelectronic simulation. All calculations were made at $T = 298$ K.

For a specific value of N_f^s, we used Eq. (7) to determine the carrier lifetimes in the CIGS or CZTSSe layer as

$$\left.\begin{array}{l} \tau_n^s = \frac{1}{\sigma_n^s v_{th}^s N_f^s} \\ \tau_p^s = \frac{1}{\sigma_p^s v_{th}^s N_f^s} \end{array}\right\}, \tag{8}$$

so the recombination rates in that layer are given as

$$\left.\begin{array}{l} R_{rad}^s(n, p; z) = R_B^s[n(z)p(z) - (n_i^s)^2] \\ R_{SRH}^s(n, p; z) = \frac{n(z)p(z) - (n_i^s)^2}{\tau_p^s[n(z)+n_1(z)] + \tau_n^s[p(z)+p_1(z)]} \end{array}\right\}. \tag{9}$$

For a specific value of ξ (and therefore E_g^s), we used

$$n_i^s = \sqrt{N_c^s N_v^s}\,\exp(-\mathsf{E}_g^s/2k_B T) \tag{10}$$

emerging from Eq. (5). Note that the electron affinity

$$\chi^s = 4.5 - 0.6\xi\ (\text{eV}) \tag{11}$$

and the bandgap energy

$$\mathsf{E}_g^s = 0.947 + 0.679\xi\ (\text{eV}) \tag{12}$$

for CIGS PVSCs.[30,63] Likewise, for CZTSSe PVSCs, we used

$$\chi^s = 4.46 - 0.16\xi\ (\text{eV}) \tag{13}$$

but

$$\mathsf{E}_g^s = 0.91 + 0.58\xi\ (\text{eV}) \tag{14}$$

for optical calculations and

$$\mathsf{E}_g^s = 0.91 + 0.44\xi\ (\text{eV}) \tag{15}$$

for electrical calculations.[4,10] The bandgap energy of CZTSSe is artificially reduced for electrical calculations to account for bandtail states.

3 Results and Discussion

3.1 CIGS Thin-Film Solar Cells

3.1.1 *Defect density*

We begin with simulations of CIGS thin-film PVSCs with $\xi \in [0,1]$ and $N_f^s \in [10^{11}, 10^{16}]$ cm^{-3}, with $N_A^s = 2 \times 10^{16}$ cm^{-3} and $L_s = 2200$ nm being fixed. Also for CIGS, we set $N_c^s = 6.8 \times 10^{17}$ cm^{-3}, $N_v^s = 1.5 \times 10^{19}$ cm^{-3}, $R_B^s = 10^{-10}$ cm^3 s^{-1}, $\sigma_n^s = 5 \times 10^{-13}$ cm^2, $\sigma_p^s = 10^{-15}$ cm^2, and $v_{th}^s = 10^7$ cm s^{-1}. Contour plots of η, J_{sc}, V_{oc}, and FF as functions of ξ and N_f^s are presented in Fig. 2.

Figure 2(a) shows that η decreases with increasing N_f^s for any fixed value of ξ. In contrast, η first increases to a maximum as ξ increases from zero to ~0.7 and then decreases with further increases of ξ toward unity for any fixed value of N_f^s. The lowest value of η is found for $\xi = 0$ (i.e., the lowest value of E_g^s) and the highest value of N_f^s.

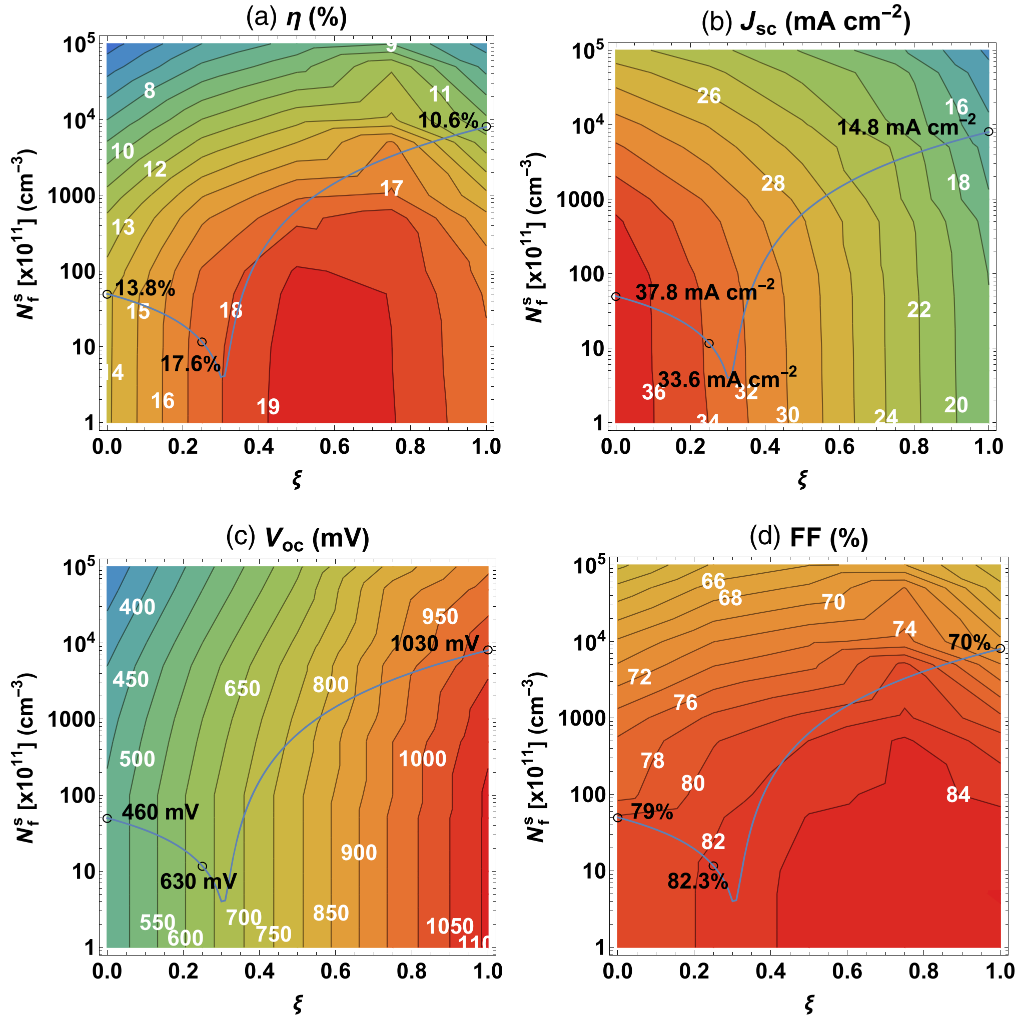

Fig. 2 Contour plots of (a) η, (b) J_{sc}, (c) V_{oc}, and (d) FF as functions of ξ and N_f^s for a CIGS thin-film PVSC, when $N_A^s = 2 \times 10^{16}$ cm^{-3} and $L_s = 2200$ nm; see Sec. 3.1.1 for other CIGS parameters. The small open circles show the values measured for experimentally realized CIGS solar cells for $\xi \in \{0, 0.25, 1\}$.[70,71] The blue solid lines represent Eq. (16).

According to Figs. 2(b) and 2(c), J_{sc} decreases but V_{oc} increases as ξ increases from zero to unity for fixed N_f^s; but both J_{sc} and V_{oc} decrease as N_f^s increases for fixed ξ. The fill factor increases as ξ increases for fixed N_f^s, and it decreases as N_f^s increases for fixed ξ. The maximum J_{sc} of 37.5 mA cm^{-2} requires $\xi = 0$, the maximum V_{oc} of 1110 mV corresponds to $\xi = 1$, and the maximum FF requires $\xi = 1$. The highest J_{sc} for the lowest ξ (i.e., lowest E_g^s) and the highest V_{oc} for the highest ξ are in accord with theory.[34]

N_f^s and ξ are treated as independent variables for the simulations resulting in Fig. 2, whereas N_f^s must depend on ξ for actual solar cells. We decided to match experimental results to our simulation results to model N_f^s as a function of ξ. Values of J_{sc}, V_{oc}, FF, and η obtained from optoelectronic simulations for $\xi = 0$ ($\mathsf{E}_g^s = 0.947$ eV), $\xi = 0.25$ ($\mathsf{E}_g^s = 1.12$ eV), and $\xi = 1$ ($\mathsf{E}_g^s = 1.626$ eV), as well as the corresponding experimental data, are provided in Table 1.[55,70,71]

The simulated values of η corresponding to experimental data points at $\xi \in \{0, 0.25, 1\}$ are marked with the small circles along with the printed η values in Fig. 2(a). The corresponding values of N_f^s are 5×10^{12} cm^{-3}, 1.16×10^{12} cm^{-3}, and 8×10^{14} cm^{-3}, respectively, emerge from optoelectronic simulations. In the absence of other experimental data for PVSCs with 2200-nm-thick CIGS photon-absorber layer, we have just three points to fit N_f^s to ξ.

The most elaborate polynomial fit then can only be of the second order. A simple quadratic fit yielded $N_f^s < 0$ for a ξ-range, which was rejected as it is physically impossible. We elected to

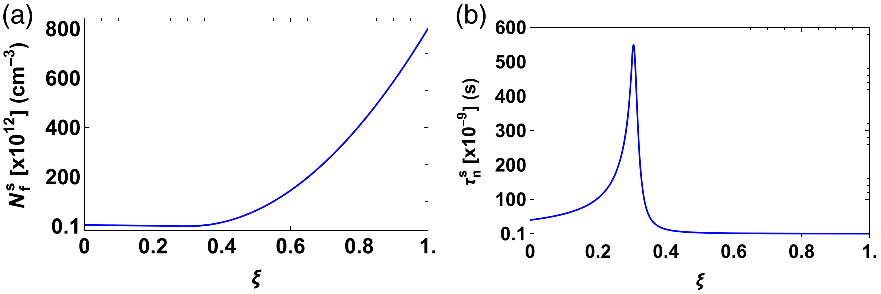

Fig. 3 (a) $N_{\rm f}^{\rm s}$ and (b) $\tau_{\rm n}^{\rm s}$ as functions of ξ obtained using Eqs. (8) and (16) for CIGS thin-film PVSCs.

use a piecewise-quadratic fit, one piece being $0 \le \xi < \tilde{\xi}$ and the other $\tilde{\xi} < \xi \le 1$ with $\tilde{\xi} \in (0,1)$; in addition, both $N_{\rm f}^{\rm s}$ and $dN_{\rm f}^{\rm s}/d\xi$ should be continuous at $\xi = \tilde{\xi}$ for physical reasons. Finally, because $N_{\rm f}^{\rm s}$ is known to be minimum when $\xi \approx 0.3$,[25] we set $\tilde{\xi} = 0.3$. The most appropriate fit that we found to satisfy all of these requirements is

$$N_{\rm f}^{\rm s} = 10^{12} \times \begin{cases} 5 - 15.33\xi, & \xi \in [0, 0.3], \\ 153.83 - 1007.57\xi + 1653.74\xi^2, & \xi \in [0.3, 1], \end{cases} \tag{16}$$

with $N_{\rm f}^{\rm s}$ carrying the unit of cm^{-3}.

Figure 3(a) shows that $N_{\rm f}^{\rm s}$ decreases linearly as the gallium fraction ξ increases from zero to 0.3 and then increases quadratically for further increases of ξ. Not only does Eq. (16) deliver simulated values of η that are reasonably close to their experimental counterparts, but it also delivers reasonable values of $J_{\rm sc}$, $V_{\rm oc}$, and FF also. Although some variance of $N_{\rm f}^{\rm s}$ from Eq. (16) can be acceptable for simulations because of the experimental variability exemplified through Table 1, too much variance could result in incorrect predictions of η, $J_{\rm sc}$, $V_{\rm oc}$, and FF. Plots of $J_{\rm dev}$ versus $V_{\rm ext}$ of CIGS thin-film solar cells for $\xi \in \{0, 0.25, 1\}$ are shown in Fig. 4(a). The numerical values of the maximum $J_{\rm dev}$-$V_{\rm ext}$ product (power density) for each value of ξ are also identified.

Because Eq. (16) conforms to the experimental data reasonably well without using surface defects,[69] so all performance parameters of CIGS thin-film PVSCs can be predicted using only the bulk material-response parameters. Equation (16) helps model the defect density in graded-bandgap CIGS solar cells[69] and can be expected to do the same for quantum-well-based CIGS solar cells,[50] thereby assisting experimentalists.

3.1.2 *Minority carrier lifetime*

It is commonplace to use the minority carrier lifetime to model the SRH recombination process instead of the defect density. This is because of the great disparity between $\tau_{\rm n}^{\rm s}$ and $\tau_{\rm p}^{\rm s}$, arising

Table 1 Comparison of $J_{\rm sc}$, $V_{\rm oc}$, FF, and η predicted by optoelectronic simulations of CIGS solar cells with a homogeneous CZTSSe layer with their experimental counterparts.[55,70,71]

ξ	$E_{\rm g,min}$ (eV)		$J_{\rm sc}$ (mA cm^{-2})	$V_{\rm oc}$ (mV)	FF (%)	η (%)
0	0.95	Model	37.79	460	79	13.79
		Experiment (Ref. 70)	40.58	491	66	14.5
		Experiment (Ref. 70)	41.10	491	75	15.0
0.25	1.12	Model	33.95	630	82	17.64
		Experiment (Ref. 71)	35.22	692	79	19.5
		Experiment (Ref. 55)	37.8	741	81	22.60
1	1.626	Model	14.78	1030	70	10.66
		Experiment (Ref. 70)	14.88	823	71	9.53
		Experiment (Ref. 70)	18.61	905	75	10.20

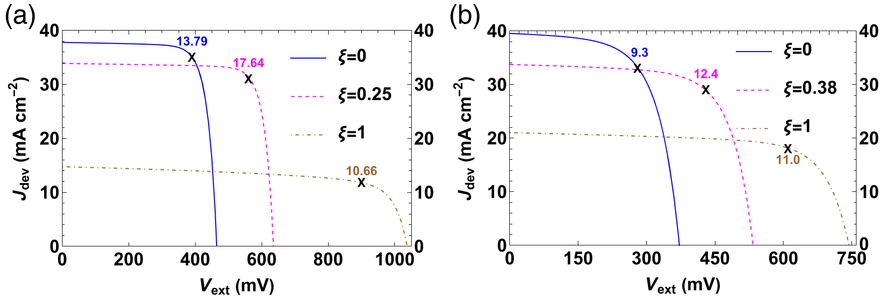

Fig. 4 (a) Plots of J_{dev} versus V_{ext} of CIGS thin-film solar cells for $\xi \in \{0, 0.25, 1\}$ and (b) plots of J_{dev} versus V_{ext} of CZTSSe thin-film solar cells for $\xi \in [0, 0.38, 1]$. The numerical values of the maximum product $J_{\text{dev}} V_{\text{ext}}$ (power density) for each value of ξ are also identified.

from the great disparity between σ_n^s and σ_p^s. In CIGS, electrons are the minority charge carriers and $\tau_n^s = 0.002\tau_p^s$, indicating that the electron lifetime limits the SRH recombination rate. Equations (8) and (16) were combined to deliver τ_n^s as a function of ξ in Fig. 3(b).

Contour plots of η, J_{sc}, V_{oc}, and FF as functions of ξ and τ_n^s are presented in Fig. 5. All four performance parameters increase as the minority carrier lifetime increases, for all values of ξ. The lowest value of η is found for $\xi = 0$ (i.e., lowest E_g^s) and the lowest value of τ_n^s.

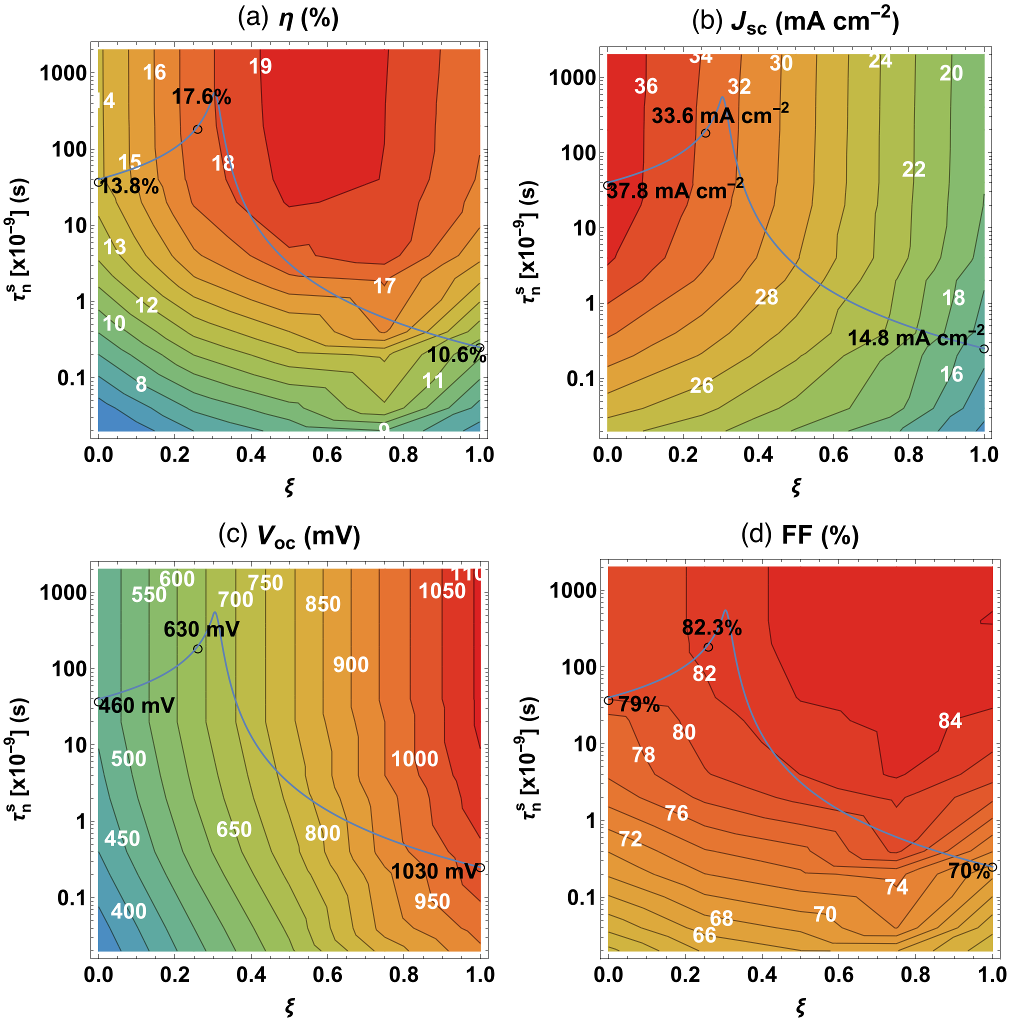

Fig. 5 Contour plots of (a) η, (b) J_{sc}, (c) V_{oc}, and (d) FF as functions of ξ and τ_n^s for a CIGS thin-film PVSC, when $N_A^s = 2 \times 10^{16}$ cm^{-3} and $L_s = 2200$ nm. The small open circles show the values of the experimentally realized CIGS solar cells for $\xi \in \{0, 0.25, 1\}$. The blue solid lines show τ_n^s as functions of ξ obtained using Eqs. (8) and (16).

3.1.3 *Effect of doping density*

Once Eq. (16) has been settled using experimental data, the effect of the doping density $N_{\rm d}(z)$ in the photon-absorber layer on the solar-cell performance can be investigated. Because the CIGS layer is homogeneous, $N_{\rm d}(z) = -N_{\rm A}^{\rm s}$ in that layer. Using Eq. (16) for $N_{\rm f}^{\rm s}$ and fixing $L_{\rm s} = 2200$ nm, we varied $\xi \in [0,1]$ and $N_{\rm A}^{\rm s} \in [10^{13}, 5 \times 10^{17}]$ cm^{-3}, all other parameters being the same as for Fig. 2. Contour plots of η, $J_{\rm sc}$, $V_{\rm oc}$, and FF as functions of ξ and $N_{\rm A}^{\rm s}$ are presented in Fig. 6.

Figure 6(a) shows that η first increases to a maximum and then decreases as ξ increases from zero to unity for any fixed value of $N_{\rm A}^{\rm s}$. However, η increases with increasing $N_{\rm A}^{\rm s}$ when ξ is fixed at some value $\lesssim 0.7$, but η decreases with increasing $N_{\rm A}^{\rm s}$ when ξ is fixed at some value $\gtrsim 0.7$. An efficiency of 20% can be achieved with $N_{\rm A}^{\rm s} = 5 \times 10^{17}$ cm^{-3} when the gallium fraction $\xi \in [0.21, 0.34]$.

The short-circuit density in Fig. 6(b) decreases with

(i) the rise of ξ at a fixed $N_{\rm A}^{\rm s}$, which is in accord with the lower EHP generation rate with higher bandgap energy $\mathsf{E}_{\rm g}^{\rm s}$ (i.e., higher ξ) [Ref. 34, p. 95], and

(ii) the rise of $N_{\rm A}^{\rm s}$ at a fixed ξ, because the width of the depletion region in the CIGS layer decreases with higher $N_{\rm A}^{\rm s}$ [Ref. 33, p. 85].

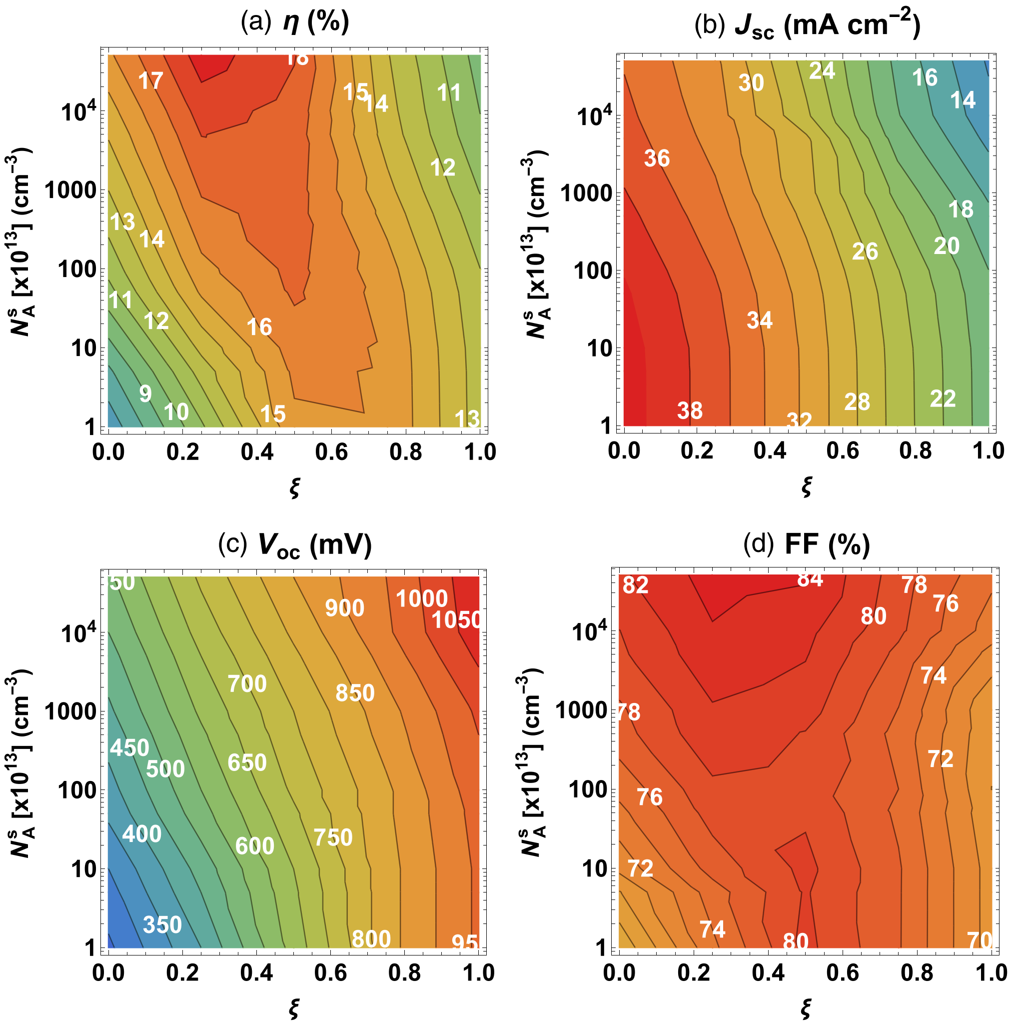

Fig. 6 Contour plots of (a) η, (b) $J_{\rm sc}$, (c) $V_{\rm oc}$, and (d) FF as functions of ξ and $N_{\rm A}^{\rm s}$ for a CIGS thin-film PVSC, when $N_{\rm f}^{\rm s}$ is given by Eq. (16) and $L_{\rm s} = 2200$ nm; see Sec. 3.1.1 for other CIGS parameters.

Similarly, the increase of V_{oc} with increasing ξ at a fixed $N_{\mathrm{A}}^{\mathrm{s}}$ is consistent with the known principle that higher $\mathsf{E}_{\mathrm{g}}^{\mathrm{s}}$ leads to higher V_{oc}.[33] Finally, FF also rises with increase in both ξ and $N_{\mathrm{A}}^{\mathrm{s}}$.

3.1.4 *Effect of CIGS layer thickness*

The thickness L_{s} of the CIGS photon-absorber layer also affects the solar-cell performance. The effects of $\xi \in [0,1]$ and $L_{\mathrm{s}} \in \{100,200,300,\ldots,2200\}$ nm on η, J_{sc}, V_{oc}, and FF, with $N_{\mathrm{f}}^{\mathrm{s}}$ given by Eq. (16) and $N_{\mathrm{A}}^{\mathrm{s}} = 10^{17}$ cm^{-3}, are shown in Fig. 7.

η increases with L_{s} for fixed ξ, whereas the efficiency first increases and then decreases as ξ increases from zero to unity. The maximum efficiency predicted is 18% with $L_{\mathrm{s}} \in [1800,2200]$ nm and $\xi \in [0.2, 0.45]$.

The short-circuit density increases with decreasing ξ and increasing L_{s}; however, the open-circuit voltage increases with increasing ξ and is affected very little by L_{s}. The fill factor increases with increasing L_{s} but decreases with increasing ξ. Higher ξ means a higher defect density and lower minority carrier lifetime [see Eq. (8)]. The diffusion length being inversely proportional to the minority carrier lifetime, a higher minority carrier lifetime allows the use of a thicker photon-absorber layer.

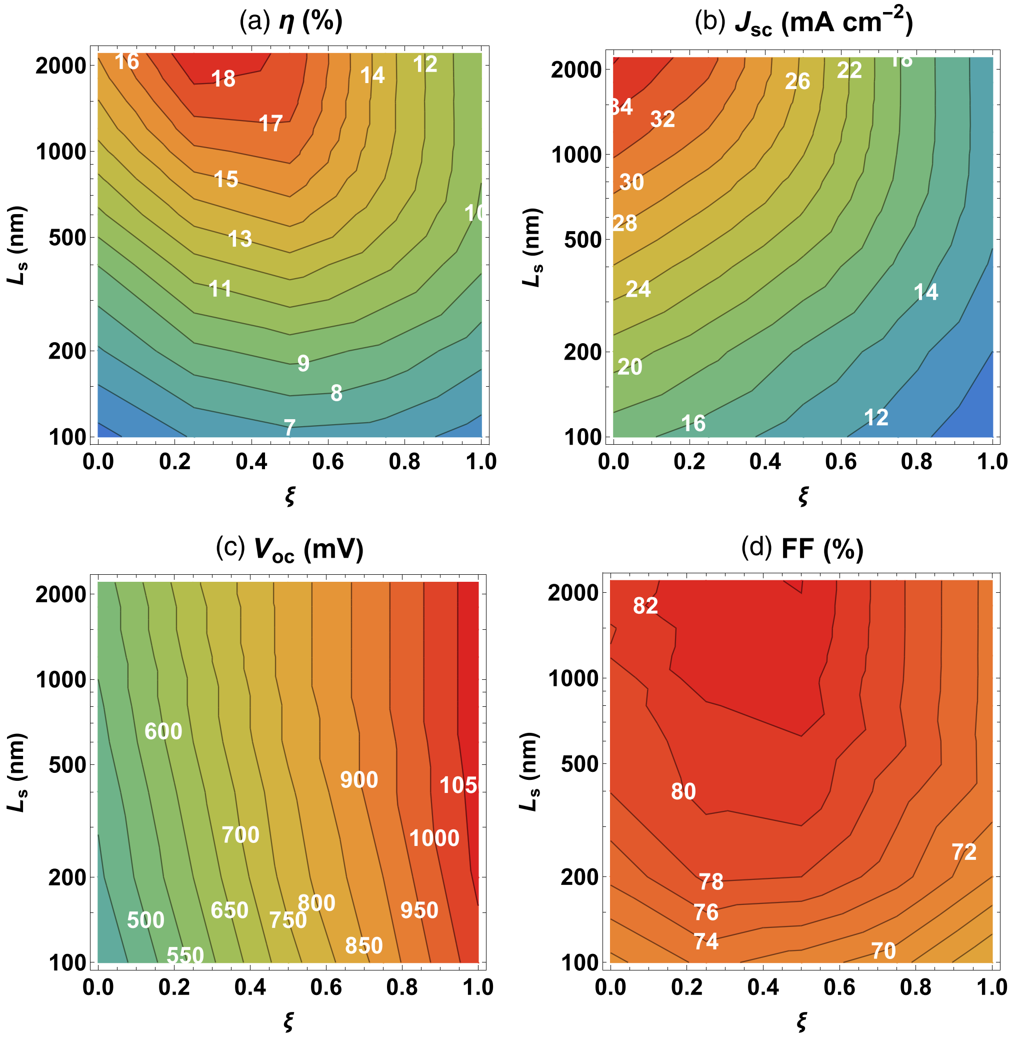

Fig. 7 Contour plots of (a) η, (b) J_{sc}, (c) V_{oc}, and (d) FF as functions of ξ and L_{s} for a CIGS thin-film PVSC, when $N_{\mathrm{f}}^{\mathrm{s}}$ is given by Eq. (17) and $N_{\mathrm{A}}^{\mathrm{s}} = 10^{17}$ cm^{-3}; see Sec. 3.1.1 for other CIGS parameters.

3.2 CZTSSe Thin-Film Solar Cells

3.2.1 *Defect density*

Little information on defect modeling with respect to bandgap variation is available in the literature on CZTSSe thin-film PVSCs. We present here a study on these devices in relation to $\xi \in [0,1]$ and $N_f^s \in [10^{11}, 10^{16}]$ cm^{-3}, with $N_A^s = 2 \times 10^{16}$ cm^{-3} and $L_s = 2200$ nm fixed. Also for CZTSSe, we set $N_c^s = 7.8 \times 10^{17}$ cm^{-3}, $N_v^s = 4.5 \times 10^{18}$ cm^{-3}, $R_B^s = 10^{-10}$ cm^3 s^{-1}, $\sigma_n^s = \sigma_p^s = 10^{-14}$ cm^2, and $v_{th}^s = 10^7$ cm s^{-1}. Contour plots of η, J_{sc}, V_{oc}, and FF as functions of ξ and N_f^s are presented in Fig. 8.

According to Fig. 8(a), the efficiency decreases with the increase of defect density and *vice versa* for fixed ξ. Also, η increases with ξ (and, therefore, E_g^s) for fixed N_f^s, in a large portion of the N_f^s-ξ space. The lowest efficiency is found for the highest N_f^s and the lowest ξ. The highest efficiency predicted is 21% for $\xi \in [0.75, 0.865]$ and $N_f^s \leq 3 \times 10^{14}$ cm^{-3}, and an efficiency higher than 20% can be achieved for $\xi \in [0.36, 1]$ (i.e., $\mathsf{E}_g \in [1.118, 1.49]$ eV) and $N_f^s \leq 10^{14}$ cm^{-3}. To achieve such high η, very high-quality CZTSSe material is needed, but that has not been experimentally possible thus far.[72–75]

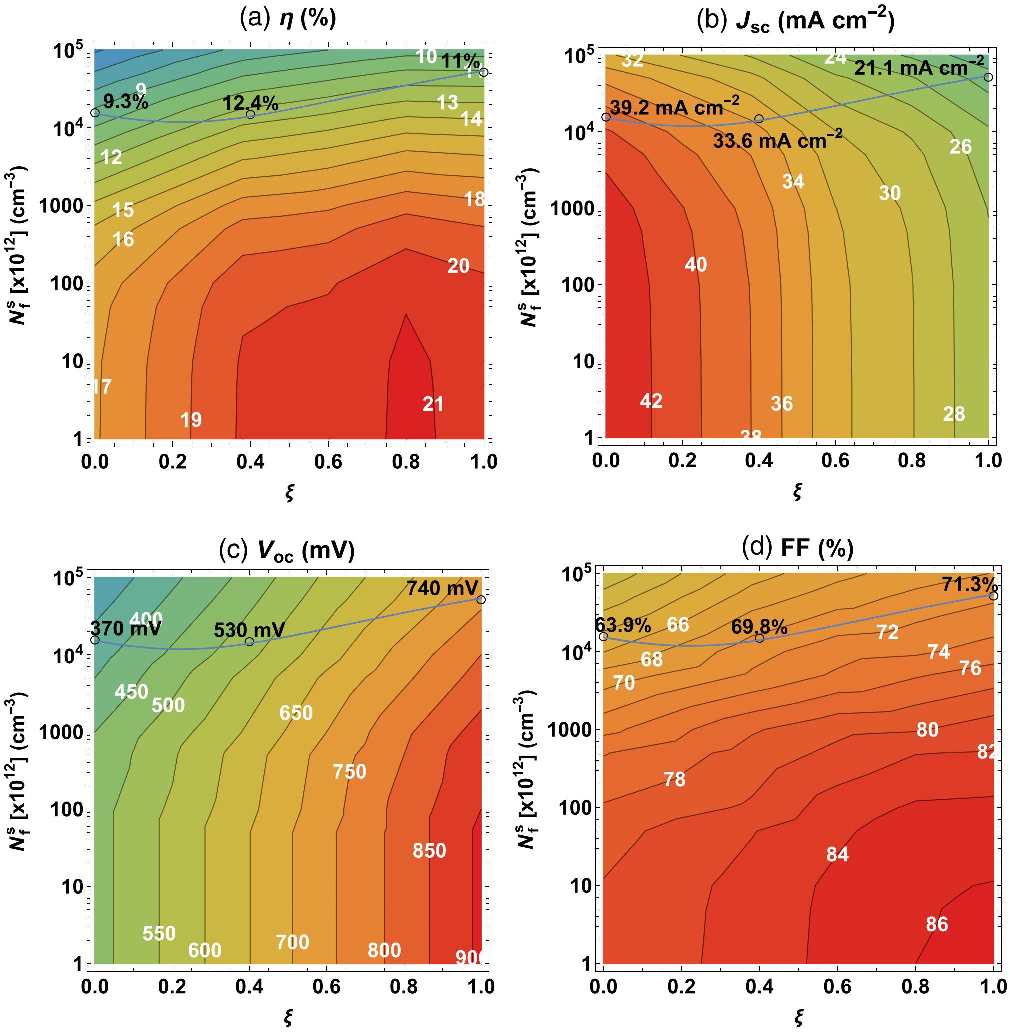

Fig. 8 Contour plots of (a) η, (b) J_{sc}, (c) V_{oc}, and (d) FF as functions of ξ and N_f^s for a CZTSSe thin-film PVSC, when $N_A^s = 2 \times 10^{16}$ cm^{-3} and $L_s = 2200$ nm; see Sec. 3.2.1 for other CZTSSe parameters. The small open circles show the values measured for the experimentally realized CZTSSe solar cells for $\xi \in \{0, 0.38, 1\}$.[72–74] The blue solid lines represent Eq. (17).

Table 2 Comparison of J_{sc}, V_{oc}, FF, and η predicted by optoelectronic simulations of CZTSSe solar cells with a homogeneous CIGS layer with their experimental counterparts.[73,74,76]

ξ	$E_{g,min}$ (eV)		J_{sc} (mA cm^{-2})	V_{oc} (mV)	FF (%)	η (%)
0	0.91	Model	39.2	370	63.9	9.3
		Experiment (Ref. 76)	36.4	412	62	9.33
0.38	1.13	Model	33.6	530	69.8	12.4
		Experiment (Ref. 73)	35.2	513.4	69.8	12.6
1	1.49	Model	21.1	740	71.3	11
		Experiment (Ref. 74)	21.74	730.6	69.27	11.01

Contour plots of J_{sc}, V_{oc}, and FF in the chosen N_f^s-ξ space are provided in Figs. 8(b)–8(d). J_{sc} decreases but V_{oc} increases with increasing ξ in accord with theory [Ref. 33, p. 31], whereas both J_{sc} and V_{oc} decrease with increasing N_f^s. The fill factor FF increases with increasing ξ but decreases with increasing N_f^s. The maximum J_{sc} of 42 mA cm^{-2} corresponds to $\xi = 0$, the maximum V_{oc} of 900 mV corresponds to $\xi = 1$, and the maximum FF of 86% also corresponds to $\xi = 1$.

So far in this section, we have treated N_f^s and ξ as independent variables for the simulations resulting in Fig. 8; however, N_f^s must depend on ξ for actual solar cells. As in Sec. 3.1.1 for CIGS thin-film PVSCs, we decided to match experimental results for CZTSSe thin-film PVSCs to our simulation results to model N_f^s as a function of ξ. Values of J_{sc}, V_{oc}, FF, and η obtained from optoelectronic simulations for $\xi = 0$ ($\mathsf{E}_g^s = 0.91$ eV), $\xi = 0.38$ ($\mathsf{E}_g^s = 1.13$ eV), and $\xi = 1$ ($\mathsf{E}_g^s = 1.49$ eV), as well as the corresponding experimental data, are provided in Table 2.[73,74,76]

The simulated values of η corresponding to experimental data points at $\xi \in \{0, 0.38, 1\}$ are marked with small circles along with the printed η values in Fig. 8(a). The corresponding values of N_f^s are 1.52×10^{16} cm^{-3}, 1.4×10^{16} cm^{-3}, and 5.38×10^{16} cm^{-3}, respectively, from optoelectronic simulations. In the absence of other experimental data for PVSCs with a 2200-nm-thick CZTSSe photon-absorber layer, we have just three points to fit N_f^s to ξ. Following the criteria presented in Sec. 3.1.1 to relate N_f^s to ξ, we obtained

$$N_f^s = (1.52 - 3.07\xi + 6.93\xi^2) \times 10^{16}\ (\text{cm}^{-3}). \tag{17}$$

As also shown in Fig. 9(a), N_f^s thus decreases as the sulfur fraction ξ increases from zero to 0.4 and then increases quadratically for further increases of ξ. Equation (17) delivers not only simulated values of η that are reasonably close to their experimental counterparts but also reasonable values of J_{sc}, V_{oc}, and FF. It is expected that there can be variance in N_f^s from Eq. (17) for simulations because of experimental variability, but too much variance could result in incorrect predictions of η, J_{sc}, V_{oc}, and FF. Plots of J_{dev} versus V_{ext} of CZTSSe thin-film solar cells for $\xi \in \{0, 0.38, 1\}$ are shown in Fig. 4(b). The numerical values of the maximum J_{dev}-V_{ext} product (power density) for each case are also identified.

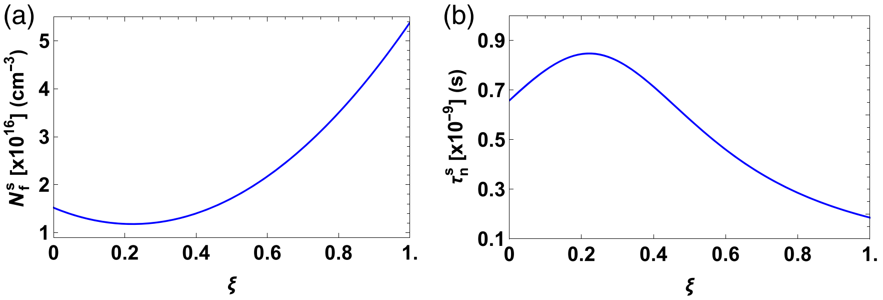

Fig. 9 (a) N_f^s and (b) τ_n^s as functions of ξ obtained using Eqs. (8) and (17) for CZTSSe thin-film PVSCs.

Similar to Eq. (16) for CIGS thin-film PVSCs, Eq. (17) conforms to the experimental parameters very well without using the surface defects; hence, all performance parameters of CZTSSe thin-film PVSCs can be reasonably predicted by just using the bulk material-response parameters. Furthermore, Eq. (17) is expected to help model the defect density in graded-bandgap and quantum-well-based CZTSSe thin-film solar cells[45,46,51,52] and better predict optimal designs for experimentalists.

3.2.2 *Minority carrier lifetime*

Equations (8) and (17) can be combined to deliver τ_n^s as a function of ξ for CZTSSe, as shown in Fig. 9(b). Contour plots of η, J_{sc}, V_{oc}, and FF as functions of ξ and τ_n^s are presented in Fig. 10. The efficiency increases with increasing minority carrier lifetime for fixed sulfur fraction ξ. For efficiency to be at least 20%, $\xi \in (0.36 - 1.0)$ and $\tau_n^s \geq 100$ ns. However, experimentally achieved values of τ_n^s remain 1 to 2 ns.[8,77] Clearly then, good-quality CZTSSe material with a low defect density and high minority lifetime is required to overcome the issue of low efficiency in CZTSSe thin-film solar cells.[78] Increased τ_n^s will increase the diffusion length and the possibility of charge-carrier collection before annihilation through the recombination processes

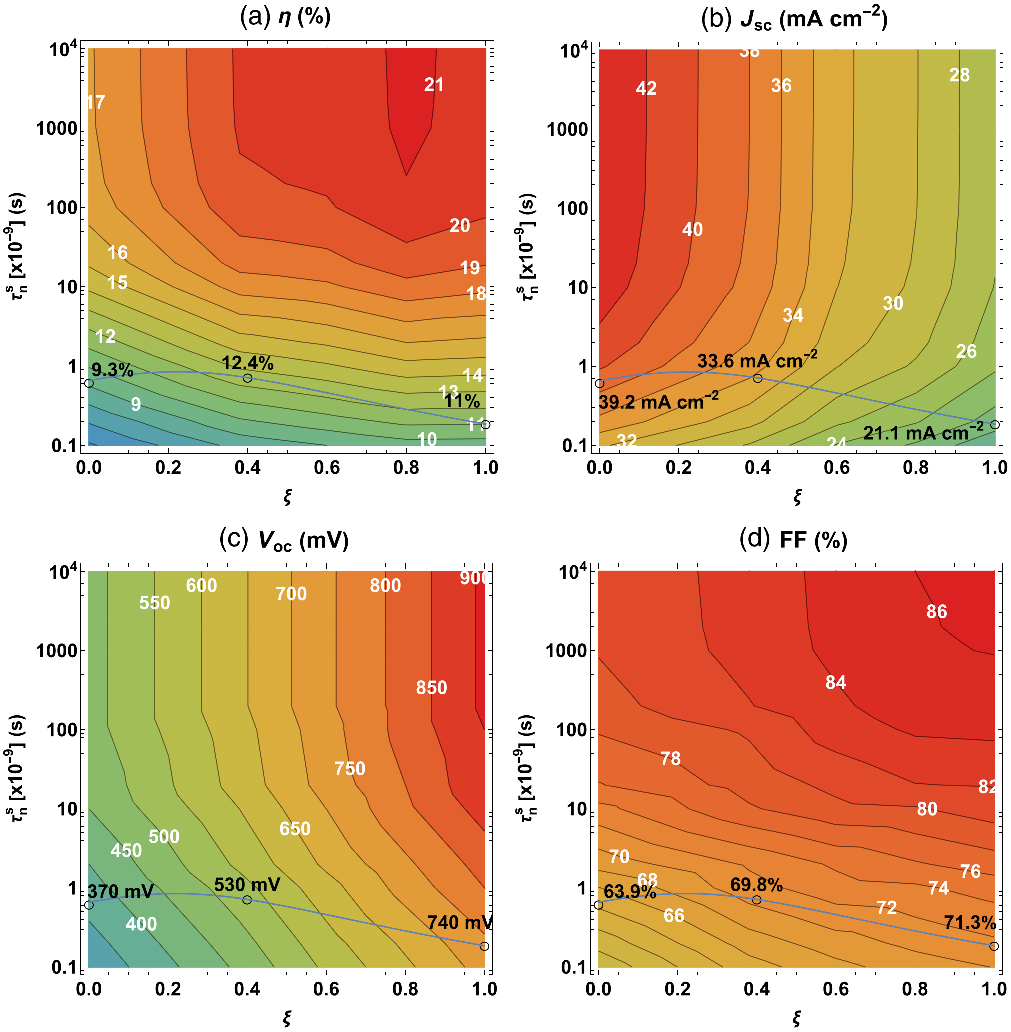

Fig. 10 Contour plots of (a) η, (b) J_{sc}, (c) V_{oc}, and (d) FF as functions of ξ and τ_n^s for a CZTSSe thin-film PVSC, when $N_A^s = 2 \times 10^{16}$ cm^{-3} and $L_s = 2200$ nm. The small open circles show the values of the experimentally realized CZTSSe solar cells for $\xi \in \{0, 0.38, 1\}$. The blue solid lines show τ_n^s as functions of ξ obtained using Eqs. (8) and (17).

[Ref. 33, p. 95]. Finally, the assumption of either very high $\tau_{\rm n}^{\rm s}$ or $\mathsf{E}_{\rm g}^{\rm s}$-independent $\tau_{\rm n}^{\rm s}$[46,47,51,52] will deliver an unreliable prediction of the device performance.

3.2.3 *Effect of doping density*

The effect of doping density $N_{\rm d}(z) = -N_{\rm A}^{\rm s}$ in the CZTSSe photon-absorber layer on the solar-cell performance was investigated using $N_{\rm f}^{\rm s}$ from Eq. (17) and fixing $L_{\rm s} = 2200$ nm. We varied $\xi \in [0,1]$ and $N_{\rm A}^{\rm s} \in [10^{13}, 5 \times 10^{17}]$ cm^{-3}, with all other parameters being the same as for Fig. 8. Contour plots of η, $J_{\rm sc}$, $V_{\rm oc}$, and FF as functions of ξ and $N_{\rm A}^{\rm s}$ are presented in Fig. 11.

Figure 11(a) shows that η first increases to a maximum and then decreases as ξ increases from zero to unity for any fixed value of $N_{\rm A}^{\rm s}$. However, as $N_{\rm A}^{\rm s}$ increases, η increases for $\xi \lesssim 0.8$ but decreases for $\xi \gtrsim 0.8$. An efficiency of 13% is possible for $N_{\rm A}^{\rm s} > 10^{16}$ cm^{-3} when $\xi \in [0.36, 0.55]$.

The short-circuit density $J_{\rm sc}$ in Fig. 11(b) decreases with increasing ξ at a fixed $N_{\rm A}^{\rm s}$, in accord with the lower EHP generation rate for higher $\mathsf{E}_{\rm g}^{\rm s}$ [Ref. 34, p. 95]. Also, $J_{\rm sc}$ decreases with increasing $N_{\rm A}^{\rm s}$ at a fixed ξ because the depletion region in the CZTSSe layer is narrower with a higher doping density [Ref. 33, p. 85]. Because higher $\mathsf{E}_{\rm g}^{\rm s}$ leads to higher $V_{\rm oc}$,[33] $V_{\rm oc}$ rises with increasing ξ at a fixed $N_{\rm A}^{\rm s}$ in Fig. 11(c). Finally, in Fig. 11(d), FF rises with increase in ξ and/or $N_{\rm A}^{\rm s}$.

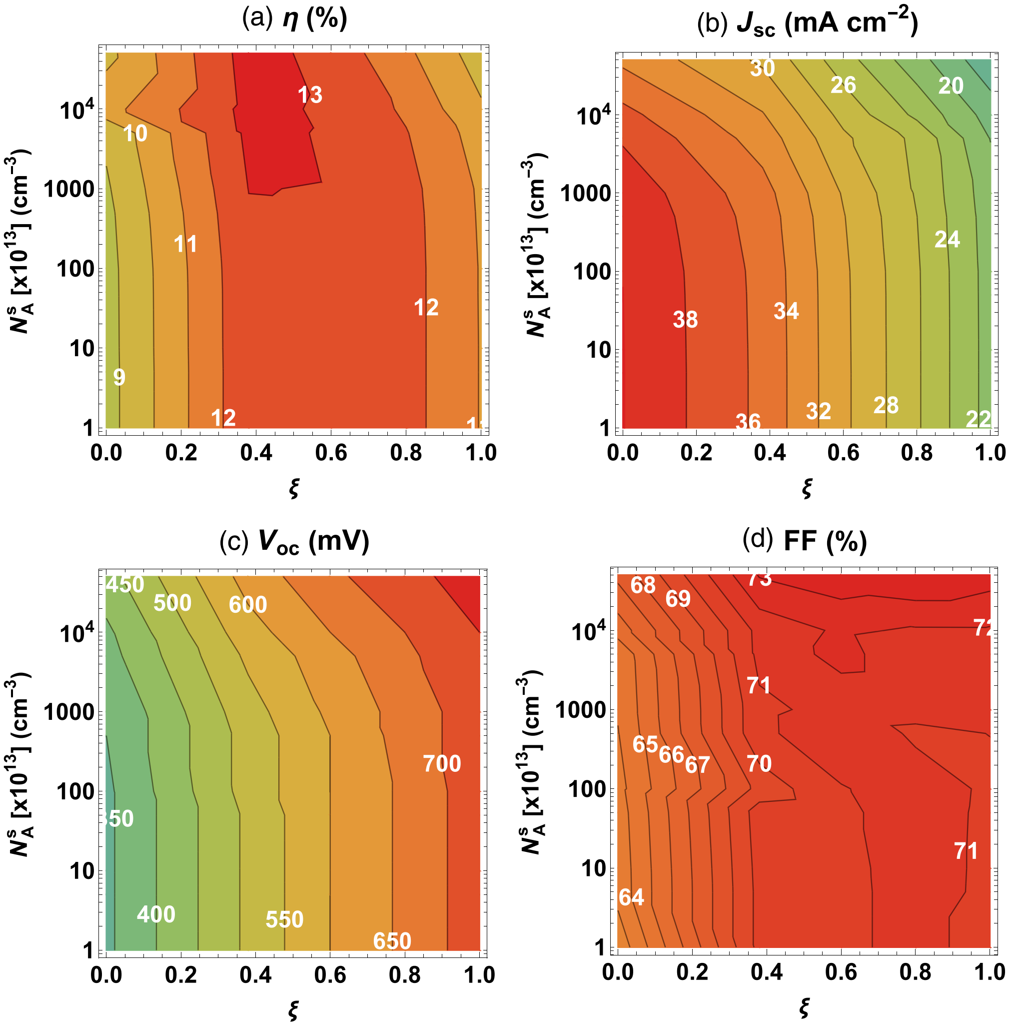

Fig. 11 Contour plots of (a) η, (b) $J_{\rm sc}$, (c) $V_{\rm oc}$, and (d) FF as functions of ξ and $N_{\rm A}^{\rm s}$ for a CZTSSe thin-film PVSC, when $N_{\rm f}^{\rm s}$ is given by Eq. (17) and $L_{\rm s} = 2200$ nm; see Sec. 3.2.1 for other CZTSSe parameters.

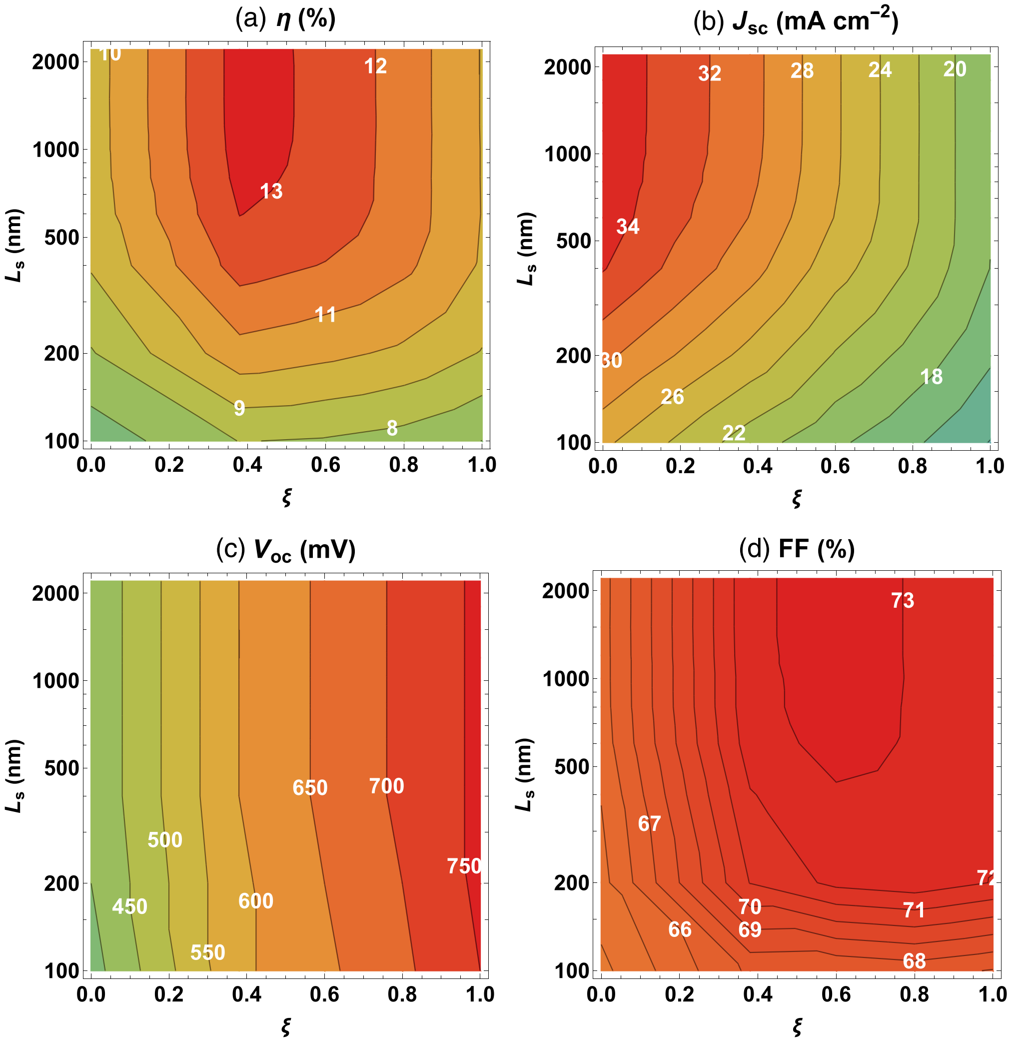

Fig. 12 Contour plots of (a) η, (b) J_{sc}, (c) V_{oc}, and (d) FF as functions of ξ and L_s for a CZTSSe thin-film PVSC, when N_f^s is given by Eq. (18) and $N_A^s = 10^{17}$ cm^{-3}; see Sec. 3.2.1 for other CZTSSe parameters.

3.2.4 *Effect of CZTSSe layer thickness*

The effects of the thickness $L_s \in [100{,}2200]$ nm of the CZTSSe photon-absorber layer on η, J_{sc}, V_{oc}, and FF, with N_f^s given by Eq. (16) and $N_A^s = 10^{17}$ cm^{-3}, are evident in Fig. 12. All of the performance parameters were evaluated for specified values of L_s in steps of 100 nm, i.e., $L_s \in \{100{,}200{,}300,\ldots,2200\}$ nm. For fixed $\xi \in [0{,}1]$, η increases with L_s initially and then it saturates, with the saturation value of L_s decreasing almost linearly with ξ. The optimal value of L_s for $\xi = 0$ (no sulfur; CZTSe) is ~1200 nm and for the $\xi = 1$ (no selenium; CZTS) is only 600 nm. Also, J_{sc}, V_{oc}, and FF saturate in the same L_s regime as does the efficiency.

An efficiency of 13% can be achieved using $L_s \approx 700$ nm and sulfur fraction $\xi \in [0.35, 0.5]$. The diffusion lengths of the electrons are directly proportional to τ_n^s and can either increase or decrease the possibility of charge-carrier collection before annihilation through the recombination processes.[33] So, the lower optimal L_s with higher ξ is a consequence of the lower diffusion length (i.e., lower carrier lifetime) of electrons in CZTSSe at higher ξ.

4 Concluding Remarks

Using optoelectronic simulations, we analyzed the effects of defect density, minority carrier lifetime, doping density, composition (i.e., bandgap energy), and absorber-layer thickness on the performances of CIGS and CZTSSe thin-film PVSCs with a homogeneous photon-absorber layer.

For solar cells of both types, we were able to formulate expressions for the defect density $N_{\mathrm{f}}^{\mathrm{s}}$ and the minority carrier lifetime $\tau_{\mathrm{n}}^{\mathrm{s}} \propto 1/N_{\mathrm{f}}^{\mathrm{s}}$ in terms of the composition parameter ξ of the homogeneous compound semiconductor in which most of the photon absorption and net conversion to charge carriers occurs. These expressions [Eqs. (16) and (17)] emerged from a comparison of limited experimental data and simulation results. All four performance parameters of the thin-films PVSCs were thereby shown to be obtainable from the bulk material-response parameters of the semiconductors, with the influence of surface defects being small enough to be ignored. Significantly, our analysis showed that the assumption of either very high $\tau_{\mathrm{n}}^{\mathrm{s}}$ or $\mathsf{E}_{\mathrm{g}}^{\mathrm{s}}$-independent $\tau_{\mathrm{n}}^{\mathrm{s}}$ will deliver an unreliable prediction of the performance of CZTSSe thin-film PVSCs, and the same conclusion could be drawn for CIGS thin-film PVSCs.

Equations (16) and (17) will guide fellow researchers in simulating the graded-bandgap and quantum-well-based CIGS and CZTSSe thin-film solar cells. Also, our systematic study on the effects of doping density and absorber-layer thickness will help to make appropriate choices for optimal designs. Finally, it can be deduced that future studies need to be focused on improving the CZTSSe quality to reach the efficiency of the CIGS thin-film PVSCs.

Acknowledgments

A. Lakhtakia thanks the Charles Godfrey Binder Endowment at Pennsylvania State University for ongoing support of his research. The research of F. Ahmad and A. Lakhtakia was partially supported by the US National Science Foundation (NSF) under Grant No. DMS-2011996. The research of P. B. Monk was supported by the US NSF under Grant No. DMS-2011603. The authors declare no conflicts of interest.

References

1. S. Almosni et al., "Material challenges for solar cells in the twenty first century: directions in emerging technologies," *Sci. Technol. Adv. Mater.* **19**, 336–369 (2018).
2. I. Massiot, A. Cattoni, and S. Collin, "Progress and prospects for ultrathin solar cells," *Nature Energy* **5**, 959–972 (2020).
3. U. P. Singh and N. B. Chaure, Eds., *Recent Advances in Thin Film Photovoltaics*, Springer, Gateway East, Singapore (2022).
4. S. Adachi, *Earth-Abundant Materials for Solar Cells*, Wiley, Chichester, West Sussex (2015).
5. C. Candelise, M. Winskel, and R. Gross, "Implications for CdTe and CIGS technologies production costs of indium and tellurium scarcity," *Prog. Photovolt.: Res. Appl.* **20**, 816–831 (2012).
6. C. Frisk et al., "Combining strong interface recombination with bandgap narrowing and short diffusion length in $\mathrm{Cu_2ZnSnS_4}$ device modeling," *Sol. Energy Mater. Sol. Cells* **144**, 364–370 (2016).
7. T. Gokmen et al., "Band tailing and efficiency limitation in kesterite solar cells," *Appl. Phys. Lett.* **103**, 103506 (2013).
8. Y. S. Lee et al., "$\mathrm{Cu_2ZnSnSe_4}$ thin-film solar cells by thermal co-evaporation with 11.6% efficiency and improved minority carrier diffusion length," *Adv. Energy Mater.* **5**, 1401372 (2015).
9. T. Gershon et al., "Understanding the relationship between $\mathrm{Cu_2ZnSn(S,Se)_4}$ material properties and device performance," *MRS Commun.* **4**, 159–170 (2014).
10. A. Kanevce, I. Repins, and S. H. Wei, "Impact of bulk properties and local secondary phases on the $\mathrm{Cu_2(Zn,Sn)Se_4}$ solar cells open-circuit voltage," *Sol. Energy Mater. Sol. Cells* **133**, 119–125 (2015).
11. I. L. Repins et al., "Indications of short minority-carrier lifetime in kesterite solar cells," *J. Appl. Phys.* **114**, 084507 (2013).
12. M. Schmid, "Review on light management by nanostructures in chalcopyrite solar cells," *Semicond. Sci. Technol.* **32**, 043003 (2017).
13. C. van Lare et al., "Light coupling and trapping in ultrathin $\mathrm{Cu(In,Ga)Se_2}$ solar cells using dielectric scattering patterns," *ACS Nano* **9**(10), 9603–9613 (2015).
14. J. Goffard et al., "Light trapping in ultrathin CIGS solar cells with nanostructured back mirrors," *IEEE J. Photovolt.* **7**, 1433–1441 (2017).
15. H. K. Raut et al., "Anti-reflective coatings: a critical, in-depth review," *Energy Environ. Sci.* **4**, 3779–3804 (2011).
16. A. Polman et al., "Photovoltaic materials: present efficiencies and future challenges," *Science* **352**, aad4424 (2016).

17. M. Gloeckler and J. R. Sites, "Band-gap grading in $\mathrm{Cu(In,Ga)Se_2}$ solar cells," *J. Phys. Chem. Solids* **66**, 1891–1894 (2005).
18. J. Song et al., "Device modeling and simulation of the performance of $\mathrm{Cu(In_{1-x},Ga_x)Se_2}$ solar cells," *Solid-State Electron.* **48**, 73–79 (2004).
19. O. K. Simya, A. Mahaboobbatcha, and K. Balachander, "Compositional grading of CZTSSe alloy using exponential and uniform grading laws in SCAPS-ID simulation," *Superlattices Microstruct.* **92**, 285–293 (2016).
20. D. Hironiwa et al., "Simulation of optimum band-gap grading profile of $\mathrm{Cu_2ZnSn(S,Se)_4}$ solar cells with different optical and defect properties," *Jpn. J. Appl. Phys.* **53**, 071201 (2014).
21. S. Mohammadnejad and A. B. Parashkouh, "CZTSSe solar cell efficiency improvement using a new band-gap grading model in absorber layer," *Appl. Phys. A* **123**, 758 (2017).
22. M. Chadel et al., "Optimization by simulation of the nature of the buffer, the gap profile of the absorber and the thickness of the various layers in CZTSSe solar cells," *Mater. Res. Express* **4**, 115503 (2017).
23. B. Vermang et al., "Employing Si solar cell technology to increase efficiency of ultra-thin $\mathrm{Cu(In,Ga)Se_2}$ solar cells," *Prog. Photovolt.: Res. Appl.* **22**, 1023–1029 (2014).
24. T. Gokmen, O. Gunawan, and D. B. Mitzi, "Semi-empirical device model for $\mathrm{Cu_2ZnSn(S,Se)_4}$ solar cells," *Appl. Phys. Lett.* **105**, 033903 (2014).
25. C. Frisk et al., "Optimizing Ga-profiles for highly efficient $\mathrm{Cu(In,Ga)Se_2}$ thin film solar cells in simple and complex defect models," *J. Phys. D: Appl. Phys.* **47**, 485104 (2014).
26. M. A. U. Khan, N. O. Adesina, and J. Xu, "Analytical modeling and design optimization of a graphene/n-GaAs Schottky junction solar cell," *J. Photonics Energy* **12**, 025502 (2022).
27. B. Farhadi et al., "Influence of the anode buffer layer materials and the light radiation power on the efficiency of a planar p-i-n perovskite solar cell: theory and simulation," *J. Photonics Energy* **12**, 015503 (2022).
28. X. Xiao et al., "Design and analysis of broadband antireflective coating for monolithic perovskite/silicon tandem solar cell," *J. Photonics Energy* **11**, 025502 (2021).
29. M. Amiri, A. Eskandarian, and A. A. Ziabari, "Performance enhancement of ultrathin graded $\mathrm{Cu(InGa)Se_2}$ solar cells through modification of the basic structure and adding antireflective layers," *J. Photonics Energy* **10**, 024504 (2020).
30. F. Ahmad, A. Lakhtakia, and P. B. Monk, *Theory of Graded-Bandgap Thin-Film Solar Cells*, Morgan & Claypool, San Rafael, California (2021).
31. S. H. Song et al., "Structure optimization for a high efficiency CIGS solar cell," in *Proc. 35th IEEE Photovolt. Special. Conf. (PVSC)*, 20–25 June, Honolulu, Hawaii, pp. 2488–2492 (2010).
32. PV Lighthouse team and contributors, "PV lighthouse," (accessed September 2022).
33. J. Nelson, *The Physics of Solar Cells*, Imperial College Press, London (2003).
34. S. J. Fonash, *Solar Cell Device Physics*, Academic Press, Burlington, Massachusetts (2010).
35. P. Bouguer, *Essai d'Optique, Sur la Gradation de la Lumière*, Calude Jombert, Paris (1729).
36. J. H. Lambert, *Photometria Sive de Mensura et Gradibus Luminis*, Colorum et Umbrae, Augsburg (1760).
37. A. Beer, "Bestimmung der Absorption des rothen Lichts in farbigen Flüssigkeiten," *Ann. Phys. Chem. Lpz.* **86**, 78–88 (1852).
38. T. G. Mayerhöfer, S. Pahlow, and J. Popp, "The Bouguer–Beer–Lambert law: shining light on the obscure," *ChemPhysChem* **21**, 2029–2046 (2020).
39. J. Billard, "Contribution a l'Etude de la Propagation des Ondes Electromagnetiques Planes dans Certains Milieux Materiels (2ème these)," PhD Dissertation, pp. 175–178, Université de Paris 6, Paris, France (1966).
40. D. W. Berreman, "Optics in stratified and anisotropic media: 4 × 4-matrix formulation," *J. Opt. Soc. Am.* **62**, 502–510 (1972).
41. T. G. Mackay and A. Lakhtakia, *The Transfer-Matrix Method in Electromagnetics and Optics*, Morgan & Claypool, San Rafael, California (2020).
42. S. M. Sze, Y. Li, and K. K. Ng, *Physics of Semiconductor Devices*, 4th ed., Wiley, Hoboken, New Jersey (2021).
43. M. Neuwirth et al., "Band-gap tuning of $\mathrm{Cu_2ZnSn(S,Se)_4}$ solar cell absorbers via defined incorporation of sulphur based on a post-sulphurization process," *Sol. Energy Mater. Sol. Cells* **182**, 158–165 (2018).
44. K. Woo et al., "Bandgap-graded $\mathrm{Cu_2ZnSn(S_{1-x},Se_x)_4}$ solar cells fabricated by an ethanol-based, particulate precursor ink route," *Sci. Rep.* **3**, 03069 (2013).
45. K.-J. Yang et al., "A band-gap-graded CZTSSe solar cell with 12.3% efficiency," *J. Mater. Chem. A* **4**, 10151–10158 (2016).
46. S. Amiri, S. Dehghani, and Roza Safaiee, "Theoretical study of graded bandgap CZTSSe solar cells with two absorber layers," *Opt. Quantum Electron.* **52**, 323 (2020).
47. S. R. F. S. Panahi et al., "Improvement of CIGS solar cell efficiency with graded bandgap absorber layer," *J. Mater. Sci: Mater. Electron.* **32**, 2041–2050 (2021).

48. F. T. Mabvuer, F. T. Nya, and G. M. D. Kenfack, “Improving the absorption spectrum and performance of CIGS solar cells by optimizing the stepped band gap profile of the multilayer absorber,” *Solar Energy* **240**, 193–200 (2022).
49. S. Yang et al., “The impact of Ga and S concentration and gradient in $\mathrm{Cu(In,Ga)(Se,S)_2}$ solar cells,” *Opt. Mater.* **126**, 112143 (2022).
50. S Azizifar et al., “Modeling of CIGS single-junction solar cell using multiple quantum well structure with enhanced efficiency,” *Opt. Quantum Electron.* **52**, 514 (2020).
51. P. Chandrasekar, S. K. Palaniswamy, and S. Routray, “Exploiting high-density Earth-abundant kesterite quantum wells for next-generation PV technology,” *IEEE Trans. Electron Dev.* **68**, 5511–5517 (2021).
52. P. Chandrasekar et al., “Determinants affecting the performance of CZTSSe: antisite defects and multiple quantum confinement for photon-sensitive devices,” *IEEE Sens. J.* **22**, 15944–15952 (2022).
53. M. Courel, J. A. Andrade-Arvizu, and O. Vigil-Galán, “Loss mechanisms influence on $\mathrm{Cu_2ZnSnS_4/CdS}$-based thin film solar cell performance,” *Solid-State Electron.* **111**, 243–250 (2015).
54. M. Courel, J.A. Andrade-Arvizu, and O. Vigil-Galán, “The role of buffer/kesterite interface recombination and minority carrier lifetime on kesterite thin film solar cells,” *Mater. Res. Express* **3**, 095501 (2016).
55. P. Jackson et al., “Effects of heavy alkali elements in $\mathrm{Cu(In,Ga)Se_2}$ solar cells with efficiencies up to 22.6%,” *Phys. Status Solidi RRL* **10**, 583–586 (2016).
56. Materion, “Transparent conductive oxide thin films,” 2012, Advanced Materials Group, https://materion.com/-/media/files/advanced-materials-group/me/technicalpapers/transparentconductiveoxidethinfilms.pdf.
57. A. B. Khatibani et al., “Characterization and gas-sensing performance of spray pyrolysed $\mathrm{In_2O_3}$ thin films: substrate temperature effect,” *Trans. Electr. Electron. Mater.* **13**, 111–115 (2012).
58. National Renewable Energy Laboratory, Reference Solar Spectral Irradiance: Air Mass 1.5 (2022).
59. M. J. Dodge, “Refractive properties of magnesium fluoride,” *Appl. Opt.* **23**, 1980–1985 (1984).
60. N. Ehrmann and R. Reineke-Koch, “Ellipsometric studies on ZnO:Al thin films: refinement of dispersion theories,” *Thin Solid Films* **519**, 1475–1485 (2010).
61. C. Stelling et al., “Plasmonic nanomeshes: their ambivalent role as transparent electrodes in organic solar cells,” *Sci. Rep.* **7**, 42530 (2017).
62. R. E. Treharne et al., “Optical design and fabrication of fully sputtered CdTe/CdS solar cells,” *J. Phys.: Conf. Ser.* **286**, 012038 (2011).
63. S. Minoura et al., “Optical constants of $\mathrm{Cu(In,Ga)Se_2}$ for arbitrary Cu and Ga compositions,” *J. Appl. Phys.* **117**, 195703 (2015).
64. F. Ahmad et al., “Optimization of light trapping in ultrathin nonhomogeneous $\mathrm{CuIn_{1-\xi}Ga_{\xi}Se_2}$ solar cell backed by 1D periodically corrugated backreflector,” *Proc. SPIE* **10731**, 107310L (2018).
65. A. Nakane et al., “Quantitative determination of optical and recombination losses in thin-film photovoltaic devices based on external quantum efficiency analysis,” *J. Appl. Phys.* **120**, 064505 (2016).
66. R. Boidin et al., “Pulsed laser deposited alumina thin films,” *Ceram. Int.* **42**, 1177–1182 (2016).
67. M. R. Querry, “Optical constants of minerals and other materials from the millimeter to the ultraviolet,” Contractor Report CRDEC-CR-88009, 1987, https://apps.dtic.mil/dtic/tr/fulltext/u2/a192210.pdf.
68. T. H. Anderson et al., “Coupled optoelectronic simulation and optimization of thin-film photovoltaic solar cells,” *J. Comput. Phys.* **407**, 109242 (2020); errata: 418109561 (2020).
69. F. Ahmad et al., “Efficiency enhancement of ultrathin CIGS solar cells by optimal bandgap grading. Part II: New algorithm and double-layer antireflection coatings,” *Appl. Opt.* **58**, 6067–6078 (2022).
70. J. AbuShama et al., “Improved performance in $\mathrm{CuInSe_2}$ and surface-modified $\mathrm{CuGaSe_2}$ solar cells,” in *Proc. 31st IEEE Photovolt. Special. Conf.*, Lake Buena Vista, Florida, pp. 299–302 (2005).
71. M. A. Contreras et al., “Diode characteristics in state-of-the-art $\mathrm{ZnO/CdS/Cu(In_{1\text{-}x}Ga)Se_2}$ solar cells,” *Prog. Photovolt. Res. Appl.* **13**, 209–216 (2005).
72. T. K. Todorov, K. B. Reuter, and D. B. Mitzi, “High-efficiency solar cell with Earth-abundant liquid-processed absorber,” *Adv. Mater* **22**, E156–E159 (2010).
73. W. Wang et al., “Device characteristics of CZTSSe thin-film solar cells with 12.6% efficiency,” *Adv. Energy Mater.* **4**, 1301465 (2014).
74. C. Yan et al., “$\mathrm{Cu_2ZnSnS_4}$ solar cells with over 10% power conversion efficiency enabled by heterojunction heat treatment,” *Nature Energy* **3**, 764–772 (2018).
75. M. A. Green et al., “Solar cell efficiency tables (Version 60),” *Prog. Photovolt. Res. Appl.* **30**, 687–701 (2022).
76. D. B. Mitzi et al., “The path towards a high-performance solution-processed kesterite solar cell,” *Sol. Energy Mater. Sol. Cells* **95**, 1421–1436 (2011).
77. T. Gershon et al., “Photoluminescence characterization of a high-efficiency $\mathrm{Cu_2ZnSnS_4}$ device,” *J. Appl. Phys.* **114**, 154905 (2013).
78. A. Polizzotti et al., “The state and future prospects of kesterite photovoltaics,” *Energy Environ. Sci.* **6**, 3171–3182 (2013).

Faiz Ahmad received his MSc and MPhil in electronics from Quaid-i-Azam University, Islamabad, Pakistan. He received his PhD in engineering science and mechanics from The Pennsylvania State University. Currently, he is a postdoctoral fellow in the Department of Engineering Science and Mechanics at The Pennsylvania State University. His research interests include electromagnetic surface waves and thin-film solar cells.

Benjamin J. Civiletti received his MA in mathematics from Villanova University and his PhD from the University of Delaware. He is an assistant professor in the Department of Mathematics and Computer Science at Augustana College. His research interests include numerical methods for modeling solar cells.

Peter B. Monk is Unidel Professor of Mathematical Sciences at the University of Delaware. He is the author of *Finite Element Methods for Maxwell's Equations* and coauthor with F. Cakoni and D. Colton of *The Linear Sampling Method in Inverse Electromagnetic Scattering*.

Akhlesh Lakhtakia received his BTech and DSc from Indian Institute of Technology and Banaras Hindu University, and his MS and PhD from the University of Utah. He is now the Evan Pugh University Professor and Charles Godfrey Binder Professor of Engineering Science and Mechanics at The Pennsylvania State University. His current research interests include nanophotonics, surface multiplasmonics, solar cells, sculptured thin films, mimumes, bioreplication, and forensic science.